

1 **Capturing the signature of heavy rainfall events using the 2-d-/4-d**
2 **water vapour information derived from GNSS measurement**
3 **in Hong Kong**

4
5 **Qingzhi Zhao**^{1,*}, **Yibin Yao**², **Wanqiang Yao**¹ and **Kefei Zhang**³

6 ¹ College of Geomatics, Xi'an University of Science and Technology, Xi'an 710054, China;
7 zhaqingzhia@163.com; sxywq@163.com

8 ² School of Geodesy and Geomatics, Wuhan University, Wuhan 430079, China; ybyao@whu.edu.cn

9 ³ School of Environment Science and Spatial Informatics, China University of Mining and Technology,
10 Xuzhou, China; kefei.zhang@rmit.edu.au

11 * Correspondence: zhaqingzhia@163.com; Tel.: +86-182-9185-5186

12
13 **Abstract:** Apart from the well-known applications like positioning, navigation and timing (PNT),
14 Global Navigation Satellite System (GNSS) has manifested its ability in many other areas that are
15 vital to society largely. With the dense setting of the regional continuously operating reference
16 station (CORS) networks, monitoring the variations in atmospheric water vapour using a GNSS
17 technique has become the focus in the field of GNSS meteorology. Most previous studies mainly
18 concentrate on the analysis of relationship between the two-dimensional (2-d) Precipitable Water
19 Vapour (PWV) and rainfall while the four-dimensional (4-d) variations of atmospheric water vapour
20 derived from the GNSS tomographic technique during rainfall events are rarely discussed. This
21 becomes the focus of this work, which investigates the emerging field of GNSS technology for
22 monitoring changes in atmospheric water vapour during rainfall, especially in the zenith direction.
23 This paper includes an analysis of both 2-d PWV and 4-d atmospheric water vapour profiles. A
24 period with heavy rainfall events in this study was selected to capture the signature of atmospheric
25 water vapour variation using the ground-based GNSS tomographic technique. GNSS observations
26 from the CORS network of Hong Kong were used. Analysed results of the 2-d PWV/4-d water
27 vapour profiles change during the arrival, occurrence and depression of heavy rainfall show that: (i)
28 the PWV time series shows an increasing trend before the arrival of heavy rainfall and decreases to
29 its average value after the depression of rainfall; (ii) rainfall leads to an anomalous variation in
30 relative humidity and temperature while their trends are totally opposite and show daily periodicity
31 for periods without rain (this is highly correlated with the changes in solar radiation); (iii)

32 atmospheric water vapour presents unstable conditions with intense vertical convective motion and
33 hydrometeors are formed before the arrival of rainfall while returning to relatively stable conditions
34 during heavy rainfall. This study indicates the potential for using GNSS-derived 2-d PWV and 4-d
35 water vapor profiles to monitor spatio-temporal variations in atmospheric water vapour during
36 rainfall, which provides a better understanding of the mechanism of convection and rainfall induced
37 by the extreme weather events.

38 **Keywords:** GNSS; PWV; water vapor profiles; extreme weather events

39

40 **1 Introduction**

41 Precipitable water vapour (PWV), which refers to the total content of integrated water vapour
42 density along the zenith direction, is a significant component reflecting the short-term atmospheric
43 water vapour variations used in severe weather detection (Shoji, 2009, 2013; Bai, 2004) as well as
44 in long-term climate studies (Gradinarsky et al., 2002, Vey et al., 2010; Ning et al., 2012; Liu et al.,
45 2013; Bock et al., 2014). However, it is difficult to obtain a satisfactory spatio-temporal resolution
46 of atmospheric water vapour due to the limitation of both the number of radiosondes and the
47 observation times (Brenot et al., 2013; Zhang et al., 2015). For the past 20 years, the ability to
48 estimate water vapour content with an accuracy of 1 to 2 mm has been proved using the Global
49 Navigation Satellite System (GNSS) technique, which generally formed a new field of study in
50 GNSS Meteorology (Bevis et al., 1992). Therefore, the variation of atmospheric water vapour with
51 high accuracy, as well as the high spatio-temporal resolution can be obtained using the hyper-dense
52 GNSS networks (with receivers only a few kilometres apart).

53 GNSS PWV can be used to provide information about water vapour distribution, which is related
54 to form of precipitation and not only to severe weather events. (Zhang et al., 2015; Yao et al., 2017;
55 Zhao et al., 2018a, 2018b). GNSS PWV is operationally used for their assimilation into numerical
56 weather prediction models (NWM) than just for operational meteorology (JMA, 2013; Bennitt and
57 Jupp, 2012; Guerova et al., 2016; Barindelli et al., 2018). In those areas, the zenith total delays (ZTD)
58 or PWV estimated from ground-based GNSS measurements are generally assimilated into
59 numerical weather prediction (NWP) (De Haan 2013; Saito et al., 2017). In addition, ZTD or PWV
60 can be used for early warnings than that it is used, which has been investigated in areas of Greater
61 Lisbon in Portugal as well as Zhejiang Province in China (Brenot et al., 2013; Benevides et al., 2015;

62 Yao et al., 2018; Zhao et al., 2018a, 2018b). These applications have verified the ability of GNSS
63 as used in meteorology, but those cases are mainly focussed on two-dimensional (2-d) PWV which
64 cannot reflect the specific vertical variations in atmospheric water vapour.

65 Although GNSS tropospheric tomography has been proposed (Flores et al., 2000), and can be used
66 to obtain four-dimensional (4-d) water vapour variations, the development of this technique has
67 mainly focussed on the improvement of theoretical and model aspects while its application is rarely
68 discussed. For example, the reliability of GNSS tomography was validated using radiosonde data
69 by Troller et al. (2006) and [Shangguan et al. \(2013\)](#). The joint reconstruction of atmospheric water
70 vapour was also investigated by combing multi-GNSS observations as well as multi-source data
71 derived from the [GNSS Radio occultation technique](#), Interferometric Synthetic Aperture Radar
72 (InSAR), radiosonde, *etc.* (Bender and Raabe, 2007; Bender et al., 2011; Wang et al., 2014;
73 Alshawaf, 2013; Heublein et al., 2015; Benevides et al., 2015; Zhao et al., 2018c). For the
74 improvement of tomographic models and resolution thereof, Perler et al. (2011) proposed a new
75 parameterised tomographic method, which is capable of obtaining better tomographic results. Some
76 methods concerned with the resolution of tomographic models have been proposed such as the
77 extended sequential successive filtering method. (Braun et al, 2003, 2004; Wang et al., 2014; Zhao
78 et al., 2017a, 2018d; Chen and Liu, 2014). In addition, maximal use of GNSS signals penetrating
79 from the side faces of tomography areas has obtained a significant improvement and is realised by
80 introducing the water vapour scale factor (Yao and Zhao, 2016; Yao et al., 2016; Zhao et al., 2017b).

81 Currently, GNSS tomography technique is maturing in terms of theoretical and model aspects
82 through almost 20 years of development, but its application in GNSS meteorology remains to be
83 further investigated, therefore, we focus on capturing the signature of heavy rainfall events using
84 the 2-d/4-d water vapour information derived from GNSS measurements in Hong Kong. The 2-d
85 PWV time series is first analysed for correlation with heavy rainfall. Thereafter, the signatures of 4-
86 d water vapour variations derived from GNSS tomography are investigated during heavy rainfall
87 events while the tomographic modelling is resolved using the optimal weighting determination
88 method.

89

90 **2 Fundamentals of GNSS meteorology**

91 **2.1 Retrieval of GNSS PWV**

92 Satellite signals are delayed and bent when crossing the troposphere, which can be divided into two
93 parts: hydrostatic delay and non-hydrostatic delay. The first part in a zenith direction, also called
94 zenith hydrostatic delay (ZHD), can be precisely calculated by the Saastamoinen model
95 (Saastamoinen, 1972) with the observed surface pressure. The second part can be estimated in the
96 zenith direction using GNSS data, which is also called zenith wet delay (ZWD), from which the
97 PWV can be calculated. Therefore, GNSS meteorology is formed, as first proposed by Bevis et al.
98 (1992). The calculation used in obtaining PWV is expressed as follows: the zenith total delay is first
99 estimated by processing the GNSS observations using the GNSS processing software such as
100 Bernese (Dach et al., 2015), GAMIT (Herring et al., 2010), etc. In the GNSS data processing, the
101 ZHD is usually taken from an a priori model and later precisely computed from i.e. real
102 meteorological observation. The ZWD is then obtained by extracting the ZHD from ZTD and thus
103 the PWV can be calculated based on the following equations (Saastamoinen, 1972; Askne and
104 Nordius, 1987; Bevis et al., 1992):

$$\begin{aligned}
& \text{PWV} = \Pi \cdot \text{ZWD} \\
& \Pi = 10^6 / \left((k_2' + k_3 / T_m) \cdot R_v \cdot \rho_w \right) \\
105 \quad & \text{ZWD} = \text{ZTD} - \text{ZHD} \tag{1} \\
& \text{ZHD} = \frac{0.002277 \times P}{1 - 0.00266 \times \cos(2\varphi) - 0.00028 \times H}
\end{aligned}$$

106 Where Π refers to the conversion factor. k_2' , k_3 , and R_v are constants with values of 22.1
107 K/hPa, 3.739×10^5 K²/hPa and 461.495 J/kg/K, respectively. T_m represents the weighted mean
108 temperature, which is related to surface parameters such as temperature and pressure. Therefore, T_m
109 is usually calculated based on the empirical model using the data from radiosonde or numerical
110 weather model due to the observed layered meteorological parameters which are rarely obtained
111 (Bevis et al., 1994; Yao et al., 2012). In the fourth formula in Eq. (1), P , H and φ represent the
112 surface pressure (hPa), geodetic height (km) and station latitude (rad), respectively. In our study, the
113 value of T_m is calculated based on the established regional T_m model using the radiosonde data and
114 observed temperature (Section 3.2).

115

116 2.2 Establishment of tomographic model

117 Generally, the slant wet delay (SWD) or slant integrated water vapour (SIWV) is considered as the

118 input information for GNSS troposphere tomography (Flores et al., 2000; Hirahara, 2000; Skone
 119 and Hoyle, 2005; Rohm and Bosy, 2009; Chen and Liu., 2014) and the following equation gives an
 120 expression used to obtain SIWV (Flores et al., 2000):

$$121 \quad \text{SIWV}_{azi,ele} = m_w(ele) \cdot \text{PWV} + m_w(ele) \cdot \cot(ele) \cdot (G_{NS}^w \cdot \cos(azi) + G_{WE}^w \cdot \sin(azi)) \quad (2)$$

122 Where m_w represents the gradient mapping function, and global mapping function (GMF) is used
 123 in our experiment (Böhm et al., 2006). ele and azi refer to the elevation angle and azimuth angle,
 124 respectively. G_{NS}^w and G_{WE}^w are the horizontal tropospheric gradient parameters of ZWD in the
 125 south-north and west-east directions, respectively, which are caused by the atmospheric
 126 inhomogeneous. Additionally, a post-fit residual for SIWV is existed, which contains some
 127 information about tropospheric water vapor distribution during the severe weather events and cannot
 128 captured by ZTD or gradients (Kacmarik et al., 2017).

129 If a sufficient number of SIWVs derived from some stations in a regional CORS network can be
 130 obtained, the GNSS tomographic technique can be used to reconstruct the three-dimensional (3-d)
 131 distribution of atmospheric water vapour field. Therefore, a four-dimensional (4-d) water vapour
 132 information is a time series of such a 3-d tomographic result, which can be used to reflect the
 133 regional atmospheric water vapour variations in both the spatial and temporal domains. As described
 134 by Flores et al. (2000), the linear observation equation between SIWV and water vapour density can
 135 be expressed as follows:

$$136 \quad \text{SIWV} = \sum (d_{ijk} \cdot x_{ijk}) \quad (3)$$

137 Where i, j and k represent the location of the area of interest in the longitudinal, latitudinal, and
 138 zenith directions, respectively. d_{ijk} and x_{ijk} refer to the distance travelled by satellite signals and
 139 the water vapour density remains to be estimated, respectively in the discretized voxels (i, j, k) .
 140 Therefore, the matrix form of the tomographic observation equation can be described as follows:

$$141 \quad \mathbf{y} = \mathbf{A} \cdot \mathbf{x} \quad (4)$$

142 Where \mathbf{y} represents the column vector of SIWV derived from GNSS measurements. \mathbf{A} and \mathbf{x}
 143 are the coefficient matrix of distance penetrated by satellite rays and the column vector of water
 144 vapour density, respectively.

145 Although Rohm (2013) developed a GNSS tomography solution using no constraints, most studies

146 still used some constraints to overcome the influence caused by the ill-posed problem in the
 147 inversion of the tomographic normal equation (Flores et al., 2000; Bi et al., 2006; Bender et al.,
 148 2011; Rohm and Bosy, 2011; Chen and Liu, 2014). In our study, both horizontal and vertical
 149 constraints are considered. The water vapour density in a certain voxel is regarded as the weighted
 150 mean value of its horizontal neighbouring voxels (Rius et al., 1997) and the negative exponential
 151 function is introduced to describe the relationship between the nearby voxels in the zenith direction
 152 while the coefficients of functional model are established using radiosonde data (Yao and Zhao,
 153 2016). Consequently, the tomographic modelling can be expressed after imposing the constraints as:

$$154 \begin{pmatrix} \mathbf{y} \\ \mathbf{0} \\ \mathbf{0} \end{pmatrix} = \begin{pmatrix} \mathbf{A} \\ \mathbf{H} \\ \mathbf{V} \end{pmatrix} \cdot \mathbf{x} \quad (5)$$

155 Where \mathbf{H} and \mathbf{V} are the coefficient matrices of horizontal and vertical equations, respectively.
 156 To obtain a reasonable tomographic result from the above equation, an optimal tropospheric solution
 157 method is used, which can adaptively tune the weightings of different types of equations (Zhao et
 158 al., 2018d).

159

160 **3 Data description and establishment of a regional T_m model**

161 **3.1 Data description**

162 To validate the ability of GNSS technique in capturing the signature of atmospheric water vapour
 163 variation during heavy rainfall events, two periods of GNSS observations (19 to 27, July 2015 and
 164 1 to 8, August 2015) from 13 GNSS stations in the CORS network of Hong Kong are selected in
 165 the experiment, which correspond to a heavy rainfall event and a no-rainfall event, respectively
 166 according to hourly rainfall data from 45 rain gauges evenly distributed across this area (Figure 1).

167 Therefore, those two periods are selected in this paper to investigate the variation characteristics of
 168 atmospheric water vapor. There is a radiosonde station located in this area where the radiosonde
 169 balloon is launched twice daily at UTC 00:00 and 12:00, respectively. The 20-years of radiosonde
 170 data from 1998 to 2017 are used to establish the regional T_m model in this study. In addition, the
 171 surface temperature and relative humidity are also selected to analyse their changes during those
 172 two periods. To explain the variations of surface temperature and relative humidity, the solar
 173 radiation data are also used in this study, which is derived from the CRU-NCEP Ver. 7 dataset (Wu

174 et al., 2015). This dataset is a combination product of the CRU TS3.2 climate dataset and the NCEP
175 reanalysis data. The temporal-spatial resolution of the solar radiation dataset are four times daily
176 (UTC 00:00, 06:00, 12:00 and 18:00) and $0.5^{\circ} \times 0.5^{\circ}$, respectively.

177 GNSS observations are processed using Precise Point Positioning (PPP) data processing software
178 developed by our research group. The post-processing mode is used and the orbit and satellite clock
179 errors are corrected using the final products downloaded from <ftp://ftp.gfz-potsdam.de/>. The GMF
180 is selected (Böhm et al., 2006) while the cut-off elevation angle is 7° in our experiment. The
181 sampling rate of GPS observation is 30s and the ZTD parameter is estimated every 5 minutes.

182 The gradient parameters in south-north and east-west directions are also estimated at intervals of 2
183 h. The detailed description of processing strategy has been presented in Zhao et al. (2018d). The
184 root-mean-square error (RMSE) of the estimated ZTD parameter has been proved with the values
185 of 7.2 mm and 8.1 mm when the ZTD estimated from the GAMIT (v10.5) and Bernese (v5.2)
186 software based on the double-difference model are regarded as references, respectively (Zhao et al.,
187 2018a). Due to the accurately ZHD parameter can be estimated using the empirical model, therefore,
188 the final error in the estimated PWV values is approximately 1-1.5mm (Zhao et al., 2018e). The
189 corresponding meteorological parameters, such as the surface pressure and temperature, are also
190 obtained at the selected GNSS stations. Therefore, the precise ZHD can be calculated by the
191 empirical model using the observed surface pressure. The conversion factor, as described in Eq. (1),
192 is also obtained, in which T_m is calculated based on the established T_m model which will be
193 introduced in the following section. Finally, the PWV time series, as well as the SIWVs for the 13
194 selected GNSS stations, can be obtained. Five of the 45 rain gauges (R21, TMS, PEN, SSP, and
195 KSC) are selected to analyse the variations in atmospheric water vapour during different weather
196 conditions (Figure 1).

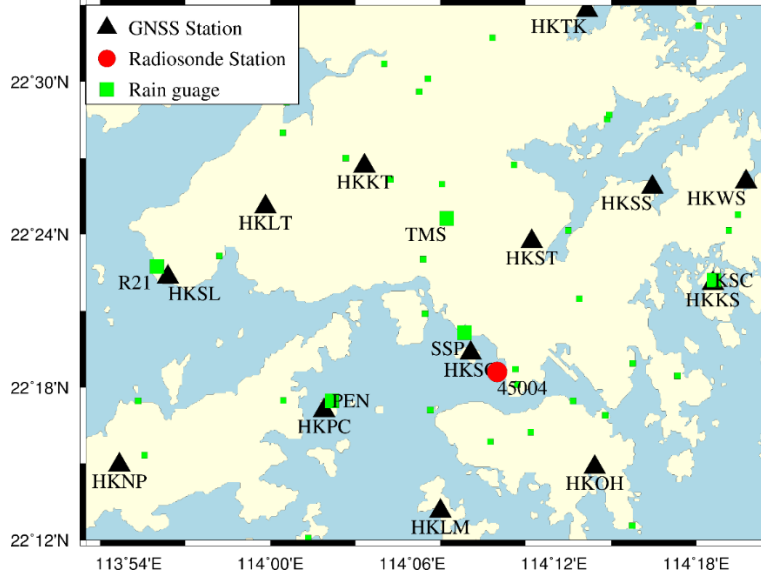


Figure 1. Geographic distribution of selected GNSS and radiosonde stations as well as the rain gauges used in the experiment

3.2 Establishment of the regional T_m model

Due to the layered information about vertical profile of some meteorological parameters as water vapour pressure or air temperature is generally unavailable for the location of GNSS stations, therefore, the T_m values of those stations are calculated based on the empirical model in this experiment. It has been proved that T_m is highly correlated with the variations of temperature, pressure, and the seasons (Bevis et al., 1992; Yao et al., 2012; Yao et al., 2014, 2015; Liu et al., 2018). Therefore, a regional T_m model which includes as parameters: temperature, surface pressure, and seasonal variation, is established and expressed as follows:

$$T_m = T_{m0} + a * T_s + b * P_s + c * \cos\left(2\pi \frac{doy}{365.25}\right) + d * \sin\left(2\pi \frac{doy}{365.25}\right) + e * \cos\left(4\pi \frac{doy}{365.25}\right) + f * \sin\left(4\pi \frac{doy}{365.25}\right) \quad (6)$$

Where T_{m0} , T_s and P_s represent the initial value of T_m , surface temperature and surface pressure, respectively; doy refers to the day of year; a and b are coefficients of T_s and P_s , respectively, while c to f refer to the coefficients of the seasonal correction function. In our study, the coefficients in Eq. (6) were obtained by the least square regression method using 20-year radiosonde data for 45004 while the values of a to f are 129.1225, 0.5370, -0.0023, 0.358, 0.813, -0.178, and 0.255, respectively.

216 The performance of the established T_m model is analysed and compared with the empirical formula
217 proposed by Bevis et al. (1994). Statistical result of 20-years of radiosonde data reveals that **when**
218 **compared to the T_m values calculated using the observed radiosonde data, the standard deviation**
219 **and bias for the established T_m model and the empirical formula proposed by Bevis et al. (1994) are**
220 **2.04/0.0009 K and 3.41/2.53 K, respectively, which indicates that the established regional T_m model**
221 **shows a good result in research area.** To further analyse the impact of T_m model error on the
222 calculated PWV, a comparison experiment is carried out for radiosonde station 45004 with a
223 variation in T_m of 1 K, 3 K, 5 K, 7 K, and 9 K, respectively and compared with the actual PWV
224 values over the period of 1998 to 2017. **Statistical analysis shows that the PWV errors induced by**
225 **the change in T_m of 1 K, 3 K, 5 K, 7 K, and 9 K are 0.15 mm, 0.45 mm, 0.75 mm, 1.04 mm, and**
226 **1.34 mm, respectively under the condition of $PWV > 0$ mm, while the values are 0.18 mm, 0.54**
227 **mm, 0.91 mm, 1.27 mm, and 1.63 mm, respectively when $PWV > 40$ mm.** Therefore, the PWV
228 errors caused by the established T_m model in this study are less than 0.4 mm and 0.5 mm when
229 $PWV > 0$ mm and $PWV > 40$ mm, respectively. Such result is deemed acceptable for the analysis
230 of PWV variations with rainfall events (Akilan et al., 2015) and **corresponds to the previous result**
231 **obtained from Guerova et al. (2016).**

232

233 **4 Signature of 2-d/4-d variations in atmospheric water vapour during rainfall**

234 According to the recordings derived from the Hong Kong Observatory, **the convective rain**
235 **happened during the period of 19 to 27, July 2015. It is continuous rains in Hong Kong and the**
236 **hourly rainfall have been accumulated for 45 rain gauges with the largest rainfall more than 300**
237 **mm for the entire experimental period in HKSC station.** The weather conditions are sunny without
238 rainfall happened for the period of 1 to 8, August 2015.

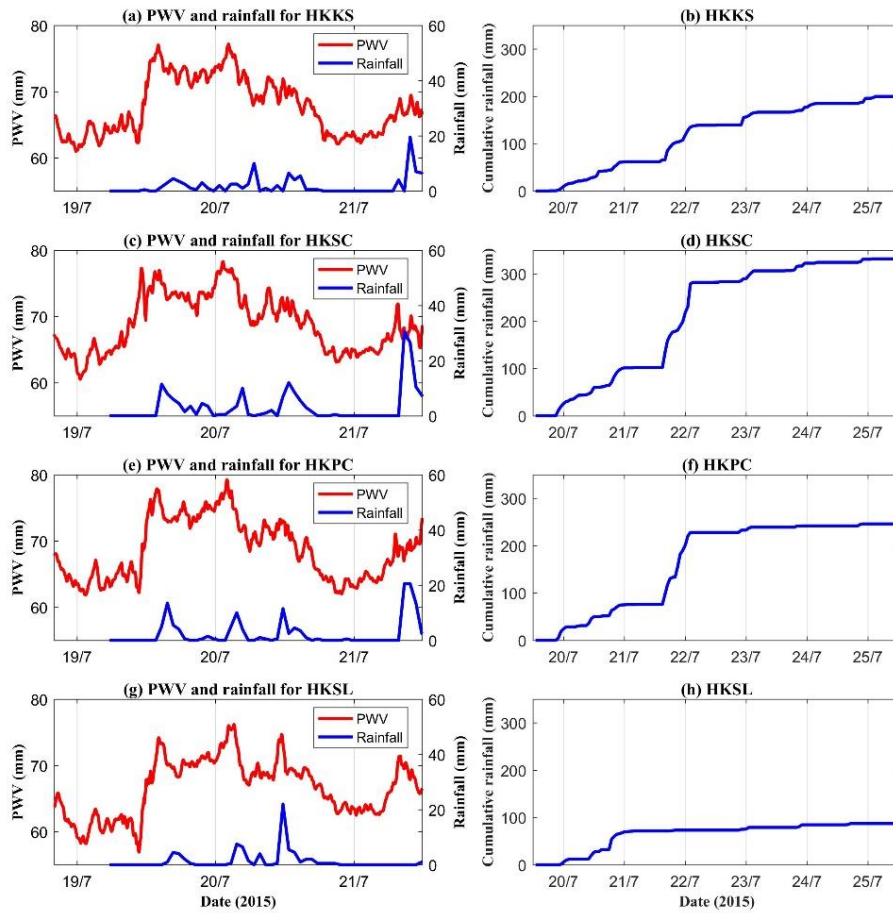
239 **4.1 Cases of 2-d PWV time series change**

240 To capture the signature of PWV time series change in different weather conditions, the comparison
241 between the 5-minute GNSS-derived PWV and hourly rainfall are performed for the periods of 19
242 to 27, July 2015 and 1 to 8, August 2015, respectively. Four GNSS stations (HKKS, HKSC, HKPC,
243 and HKSL) and the surrounding rainfall gauges (HSC, SSP, PEN, and R21) are selected for this
244 experiment. **Additionally, other meteorological parameters (temperature, relative humidity and solar**
245 **radiation) are also analysed during this experimental period.**

246 Figure 2 shows the variations of 5-minute PWV time series data with hourly rainfall (19 to 21, July
247 2015) as well as the cumulative rainfall at those four stations (19 to 27, July 2015). Here, only the
248 period of 19 to 21 were selected for PWV time series to make a clear investigation of the PWV
249 variations before the occurrence of precipitation. It can be seen from the first column of Figure 2
250 that the PWV time series show an increasing trend before the arrival of rainfall and reaches a
251 relatively large value during rainfall happened, PWV then returns to its average value after rainfall.
252 Such phenomenon found above can be used to forecast the nowcasting rainfall (Yao et al., 2017;
253 Zhao et al., 2018a). The second column of Figure 2 reveal that the cumulative rainfall first increased
254 at about UTC 11:00, 20 July, 2015 with different levels reached and the event terminated at UTC
255 12:00, 23 July, 2015. The largest cumulative rainfall reached more than 300 mm at HKSC station
256 while the minimum recorded rainfall was about 100 mm at HKSL station across the four selected
257 gauge stations. The PWV time series is also analysed at those four stations for the period from 1 to
258 8, August, 2015 in which no rainfall was recorded. The analysis of 5-minute PWV time series
259 changes reveal that PWV does not show any continuous increasing trend when there is no rainfall,
260 but the range of PWV variation is relatively large (from about 35 mm to greater than 55 mm).
261 Additionally, it also found that the PWV values during rainfall are much larger than that of no
262 rainfall time at the situation occurred in the selected time periods.

263 In addition, 5-minute surface temperature and relative humidity data are also analysed at HKKS and
264 HKSC stations during those two periods. Figure 3 (a1), (b1), (d1) and (e1) show the changes in
265 temperature and relative humidity for the period 19 to 27, July, 2015. It can be seen that the
266 temperature and relative humidity do not show any trend during heavy rainfall but show a tendency
267 to run counter to one another on 19, 26, and 27, July. one explanation is that heavy rainfall breaks
268 the trend in temperature and relative humidity for the period from 20 to 25, July, 2015. Figure 3 (c1)
269 and (f1) show the changes in solar radiation for this period, from which it can be observed that the
270 solar radiation undergoes a day periodic change. To verify this explanation, the variations of
271 temperature and relative humidity, as well as those in solar radiation, are also presented in Figure 3
272 (a2) - (f2) at those two stations for period of 1 to 8 August without rainfall: temperature and solar
273 radiation show a similar trend while relative humidity presents the opposite trend.

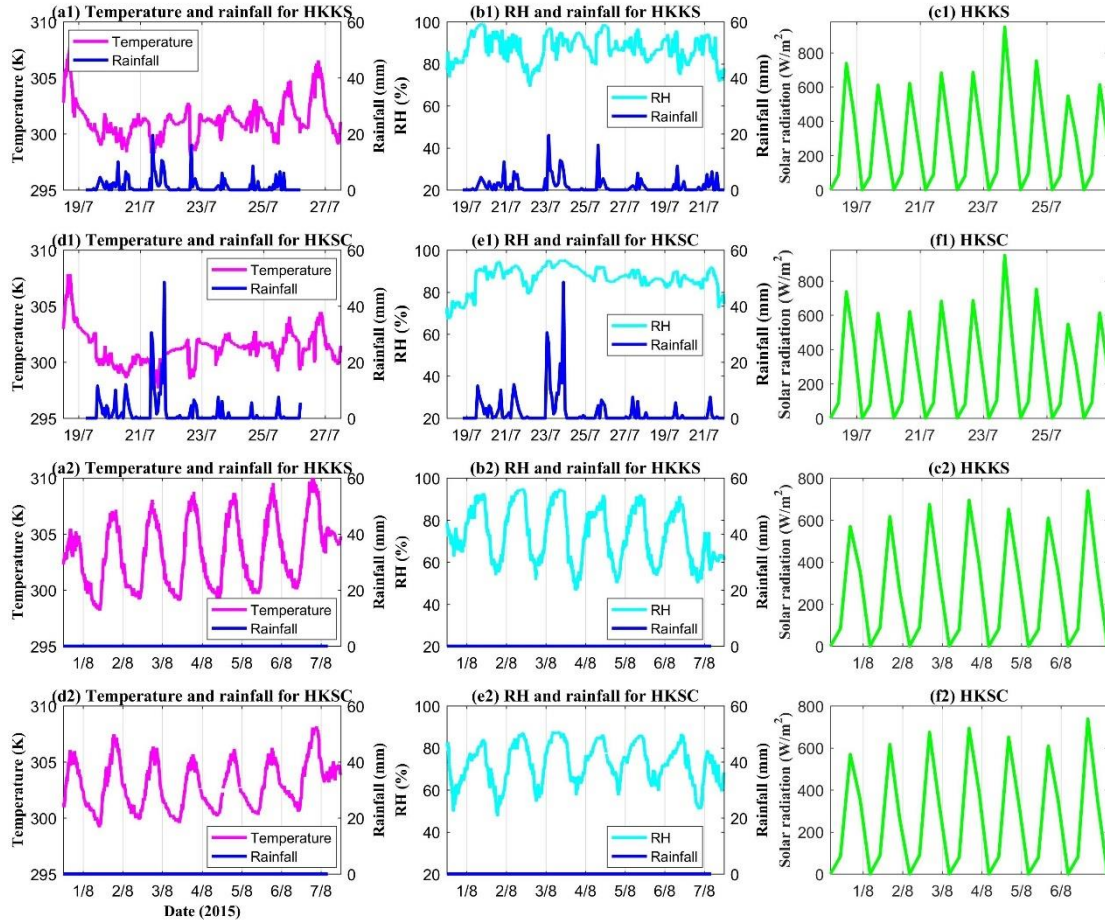
274



275

276 Figure 2. Variations of 5-minutely PWV time series with hourly rainfall over the period of 19 to
 277 21, July 2015 and the cumulative rainfall over the period of 19 to 27, July 2015, respectively, for
 278 HKKS, HKSC, HKPC and HKSL stations, the first column represents the variations of PWV and
 279 rainfall and the second column refers to the cumulative rainfall

280



281

282 **Figure 3. Changes of temperature, relative humidity with rainfall as well as the solar radiation at**
 283 **HKKS and HKSC stations over the periods of 19 to 27 July and 1 to 6 August, 2015, the first**
 284 **column represents the variations of temperature and rainfall, the second column refers to the**
 285 **variations of RH and rainfall and the third column refers to the solar radiation**

286

287 4.2 Cases of water vapour profile variation during heavy rainfall

288 The variations in 4-d atmospheric water vapour are also analysed during heavy rainfall. In this
 289 section, the tomographic technique is introduced and the research area is discretised. There are 7
 290 and 8 grids in longitudinal and latitudinal directions, respectively and 29 layers in zenith direction.
 291 Therefore, there are total $7 \times 8 \times 29$ voxels. The horizontal steps are 0.05° and 0.06° in longitudinal
 292 and latitudinal directions, respectively while the inhomogeneous vertical step is selected based on
 293 the water vapour distribution at different altitudes (Yao and Zhao, 2017) with resolutions of 0.2 km
 294 $\times 10$, $0.3 \text{ km} \times 8$, $0.4 \text{ km} \times 6$, $0.6 \text{ km} \times 4$, and $0.8 \text{ km} \times 1$, respectively. A comparison of water
 295 vapour density profiles derived from tomographic result and radiosonde data at the location of

296 radiosonde station 45004 is first presented (Figure 4) to validate the performance of the GNSS
297 tomographic technique. It can be seen from the Figure 4 that the profiles derived from tomographic
298 results were consistent with the observed radiosonde data at most altitudes, which manifests the
299 ability of the GNSS tomographic technique to reflect variations in water vapour content during
300 rainfall. Due to this paper is mainly focus on the analysis of 4-d water vapour variation during the
301 heavy rainfall events and a series of quality evaluations of vertical profiles derived from GNSS
302 tomography reconstruction have been carried out by our research group for this research area in the
303 previous studies (Yao and Zhao, 2016, 2017; Zhao et al., 2017a; Zhao et al., 2018d), therefore, more
304 detailed comparison and validation about the quality of reconstructed water vapor profiles are not
305 presented in this paper.

306 Two heavy rainfall periods are selected in this experiment: the first at UTC 18 to 22, 21 July 2015
307 and three rain gauges are used to analyse the variations in water vapour profiles. The hourly rainfall
308 for those three rain gauges is presented in Table 1 while the water vapour profile variations over
309 time for SPP, PEN and TKL are shown in Figure 5. From this figure it can be observed that
310 atmospheric water vapour profile undergoes vertical movement about 1-2 hours before the arrival
311 of heavy rain, which is reflected by the fluctuating water vapour density at different altitudes. It can
312 be observed from SPP rain gauge ((a1)-(h1)) that the water vapour content in the lower atmosphere
313 increases from an altitude of about 1.8-2.5 km to 3.5 km while the water vapour content decreases
314 from 4-5 km to 3.5 km. This similar conditions are also observed from PEN and TKL rain gauges
315 ((a2)-(h2) and ((a3)-(h3))) that an upward and downward movements happened in the atmospheric
316 water vapour profile in the lower and upper atmosphere, respectively: this results in a large increase
317 in atmosphere water vapour at altitudes of about 2.3 km and 1.6 km, respectively (especially at
318 PEN). The upward and downward motions of atmospheric water vapor in the lower and upper
319 atmosphere are expected to the occurrence of the strong convective weather. The above phenomenon
320 of vertical water vapor motion corresponds to the convectioal rain reported. In addition, it was
321 found that the variations of water vapour profiles in zenith direction at station TKL are weaker than
322 that from stations PEN and SPP. A possible explanation is that the rainfall was 30.5 mm and 20.5
323 mm for PEN and SPP at UTC 20, 21 July 2015 while the value is only 1 mm at station TKL at UTC
324 21, 21 July 2015 (Table 1). The above phenomenon indicates that the heavy rainfall could be induced
325 by the vertical motion of water vapour, which can be captured by the GNSS tomography technique.

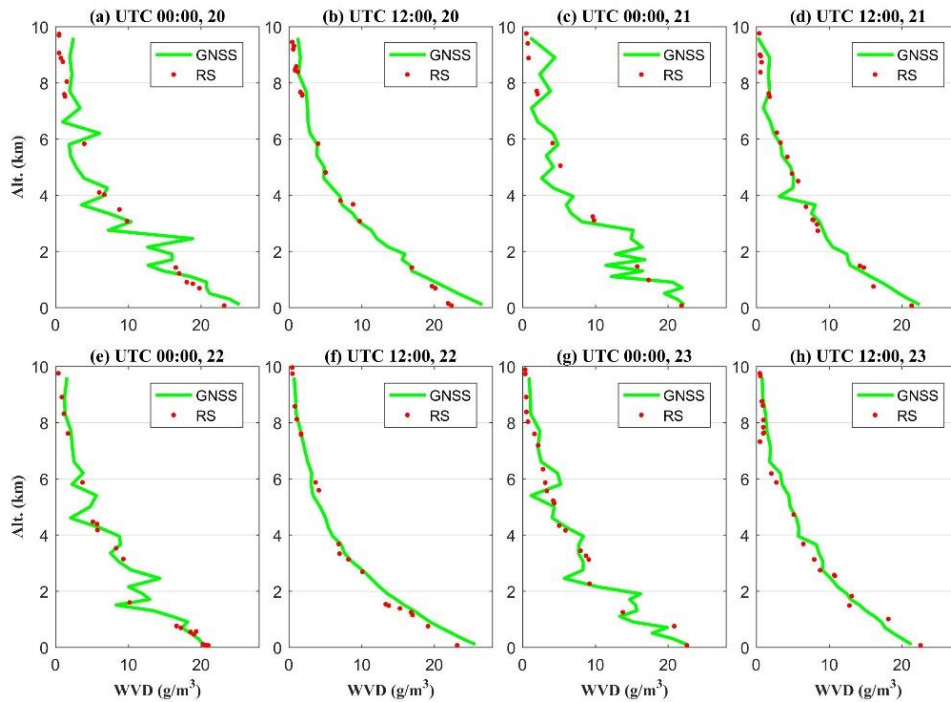
326 The variations in water vapour profiles during rainfall reveal that the significant vertical motion of
327 water vapour occurred before the onset of rainfall while the water vapour profiles were relatively
328 stable during rainfall events.

329 In addition, the time series of water vapour density profiles, at a temporal resolution of 1 minute,
330 for the three rain gauges are also presented in Figure 6. From which it can be seen that the vertical
331 water vapour density profile undergoes a significant vertical motion about 1-2 hours before the
332 arrival of rain (black dotted rectangles, Figure 6) while the profiles are relatively stable during rain.

333 This indicates that the GNSS technique is of ability to capture the variation of atmospheric water
334 vapor before the occurrence of rainfall, and has a great potential for the nowcasting and assimilation
335 in NWP. By analysing the Figure 5, it also can be found that the vertical variations of water vapour

336 density profiles at SPP and PEN stations 1 hour before rainfall are more active than that at TKL
337 station: this can be explained by considering that the continued heavy rainfall happened at SPP and

338 PEN stations while the TKL had little rainfall (Table 1), therefore, the continuing water vapour
339 transportation in the zenith direction existed in the lower atmosphere at stations SPP and PEN.



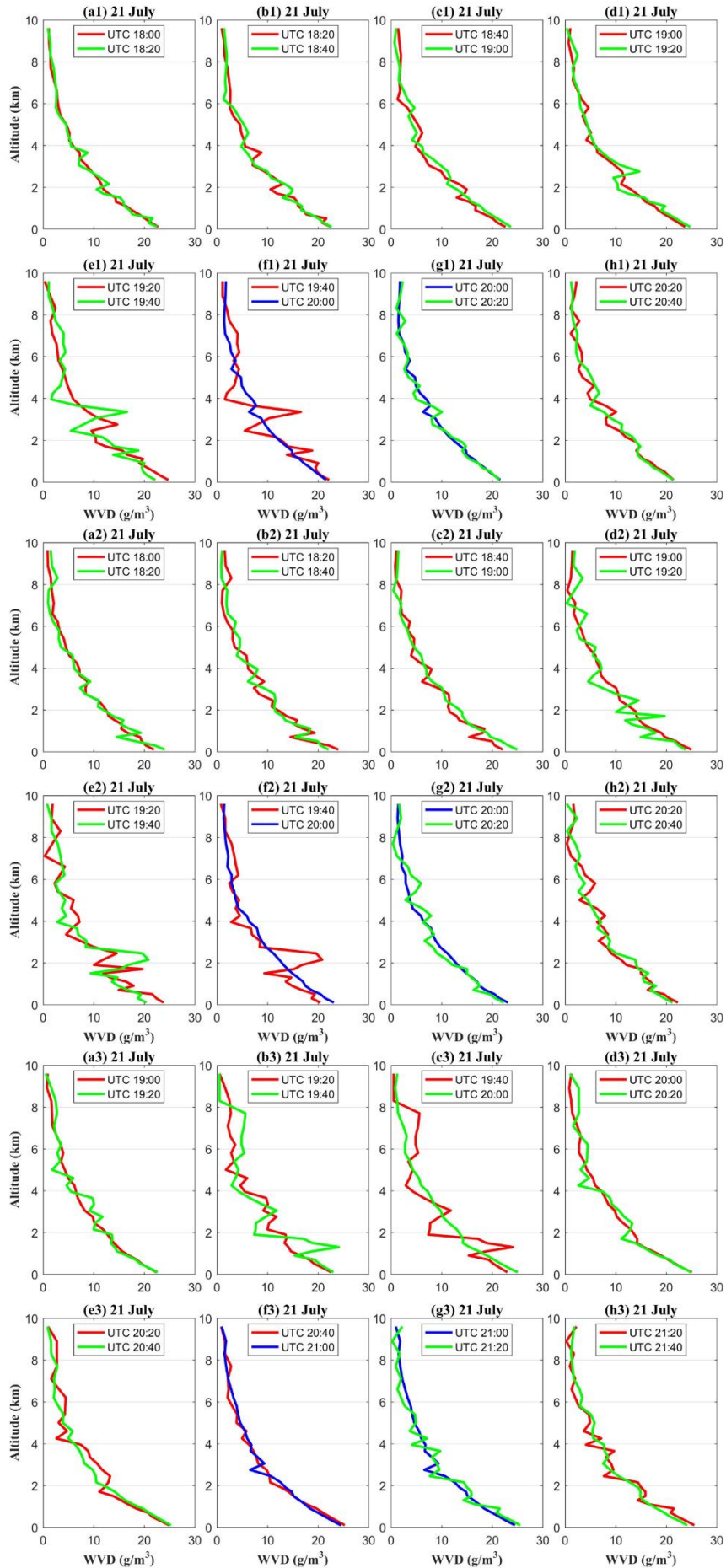
340
341 Figure 4. Distribution of water vapor density (WVD) profiles at UTC 00:00 and 12:00,
342 respectively derived from the GNSS tomographic result (green curve) and the radiosonde data of
343 the observed height (red hot) for the location of radiosonde station (45004) over the period of 20
344 to 23, July 2015

345 Table 1 Hourly Rainfall information of the selected four rain gauges over period of UTC 19 to 23,

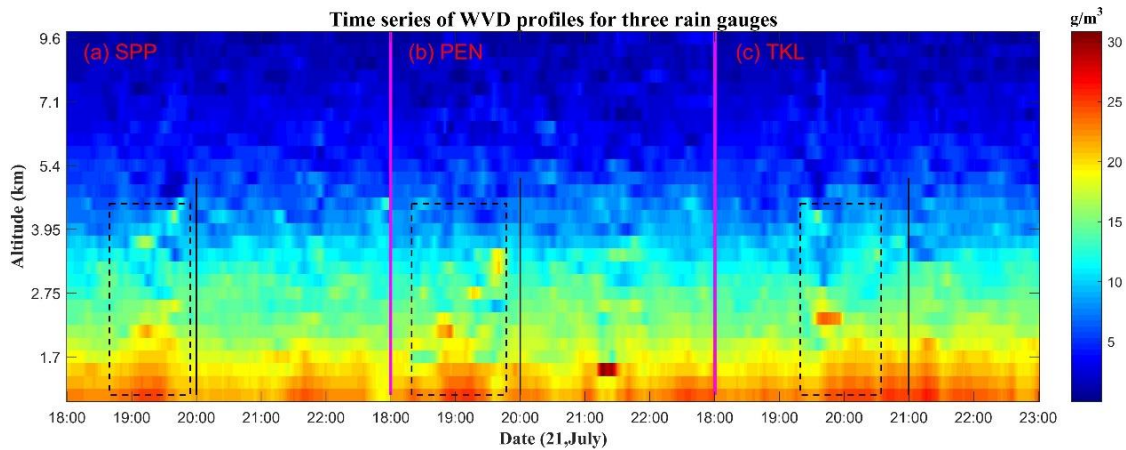
346

21 July 2015 (Unit: mm)

Station Date	SPP	PEN	TKL
19, 21 July	0	0	0
20, 21 July	30.5	20.5	0
21, 21 July	26.5	20.5	1.0
22, 21 July	10.5	13.5	1.5
23, 21 July	7.5	2.5	1.5



348 Figure 5. Distribution of water vapor density Profiles (WVD) derived from GNSS tomographic
 349 result with the temporal resolution of 20 minutes, where (a1)-(h1), (a2)-(h2) and (a3)-(h3) refer to
 350 the location of SPP, PEN and TKL rain gauge over the period of UTC 18:00-20:40, UTC 18:00-
 351 20:40 and UTC 19:00-21:40, 21 July 2015, respectively, the blue line represents the beginning
 352 epoch of precipitation



354 Figure 6. Time series of water vapor density (WVD) profiles derived from GNSS tomographic
 355 result with the temporal resolution of 1 minute for the locations of three rain gauges over the
 356 period of UTC 18:00 to 23:00, 21 July 2015, where the rainfall happened at UTC 20:00 21 July
 357 for (a) SPP and (b) PEN rain gauges while the rainfall occurred at UTC 21:00 21 July for (c) TKL
 358 rain gauge. The WVD profiles with drastic vertical motion are marked by the black dotted
 359 rectangles for three rain gauges while the locations of black solid lines are the starting time of
 360 rainfall
 361

362
 363 To verify the phenomenon observed above, another period (UTC 0 to 4, 23 July 2015) at PEN and
 364 TMS rain gauges is selected while the hourly rainfall information is presented in Table 2. Figures 7
 365 and 8 both reflect that the change in water vapour profiles at PEN and TMS stations are similar to
 366 that of above conditions. The water vapour content at PEN and TMS is increased at altitudes of 2.5
 367 km and 3.2 km, respectively, some 1-2 hours before onset of rainfall and returns to its average value
 368 at the moment that the rainfall is about to begin. One possible explanation for this is that: before
 369 onset of rainfall, the atmospheric water vapour was conditionally unstable with intense vertical
 370 movement as proved by Brenot et al., (2006). The ascending motion of atmospheric water vapour

371 in the lower atmosphere and the descending motion of water vapour in the upper atmosphere
 372 significantly increases the water vapour content at a certain height where hydrometeors are formed.
 373 The hydrometeors consist of liquid water and icy hydrometeors, formation of which is random in
 374 time and space. Due to the delays to satellite signals induced by liquid water and icy species
 375 generally being much smaller than the water vapour species-induced delays, therefore, these delays
 376 cannot be reflected evidently in the case of GNSS observations. These newly-generated
 377 hydrometeors particles form raindrops with a continual accretion thereof. When the atmosphere is
 378 unable to support the weight of the formed raindrop, the drop falls as rain. The formation of
 379 hydrometeors particles and raindrops require some time, hence the intense vertical movement of
 380 atmospheric water vapour before onset of rainfall. The time taken to generate hydrometeors and
 381 raindrops provides the possibility of now-casting rainfall based on the GNSS technique.

382

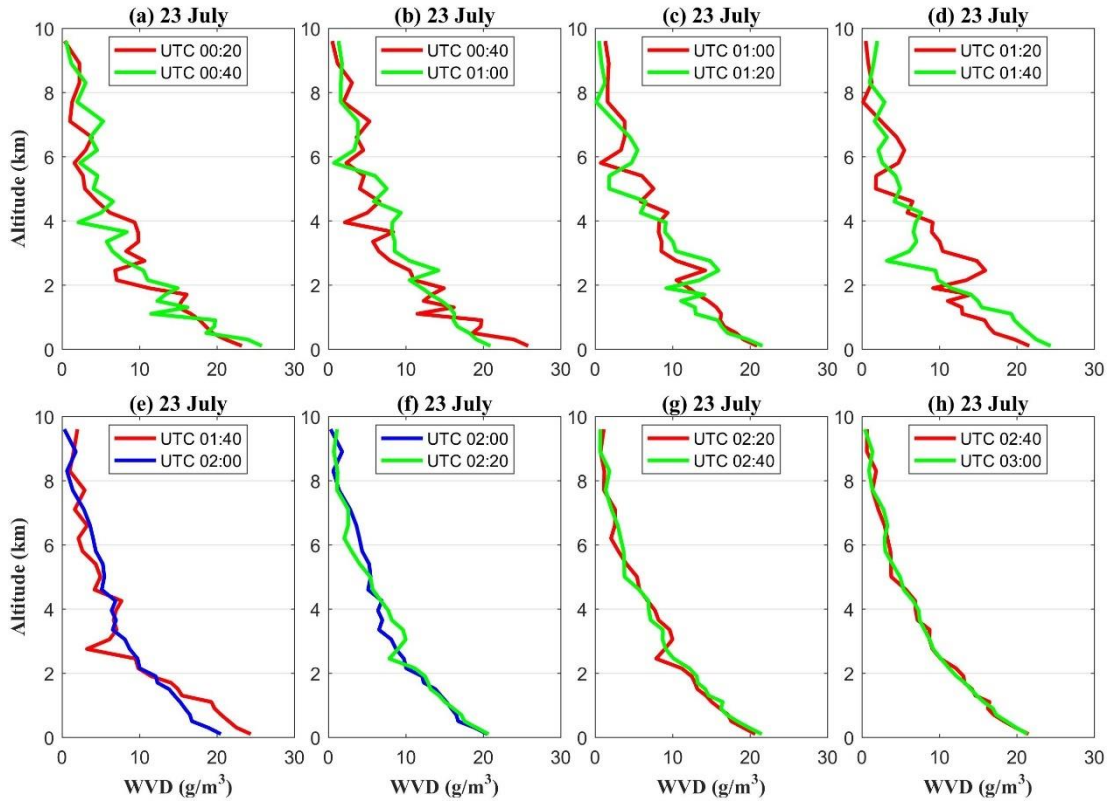
383 Table 2. Hourly Rainfall for the selected four rain gauges over the period UTC 1 to 5, 23 July

384

2015 (Unit: mm)		
Station	PEN	TMS
Date		
0, 23 July	0	0
1, 23 July	0	0
2, 23 July	4.5	16.5
3, 23 July	0.5	4.5
4, 23 July	0	0.5

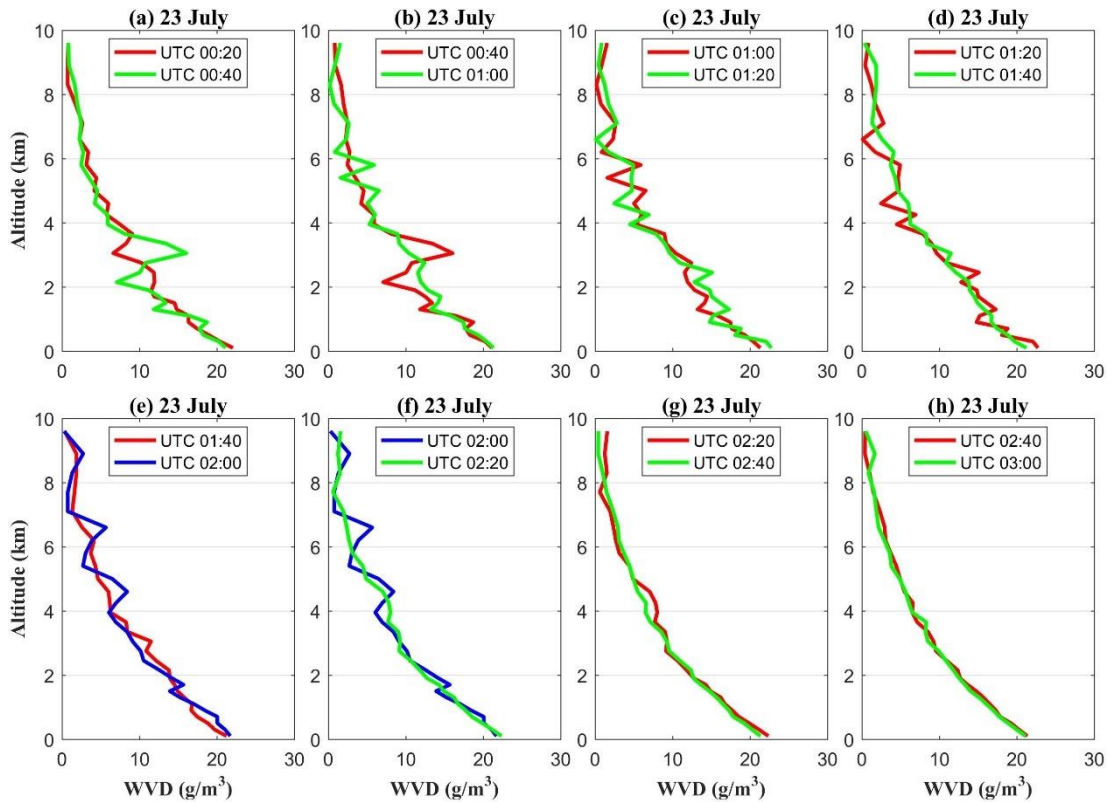
385

386



387

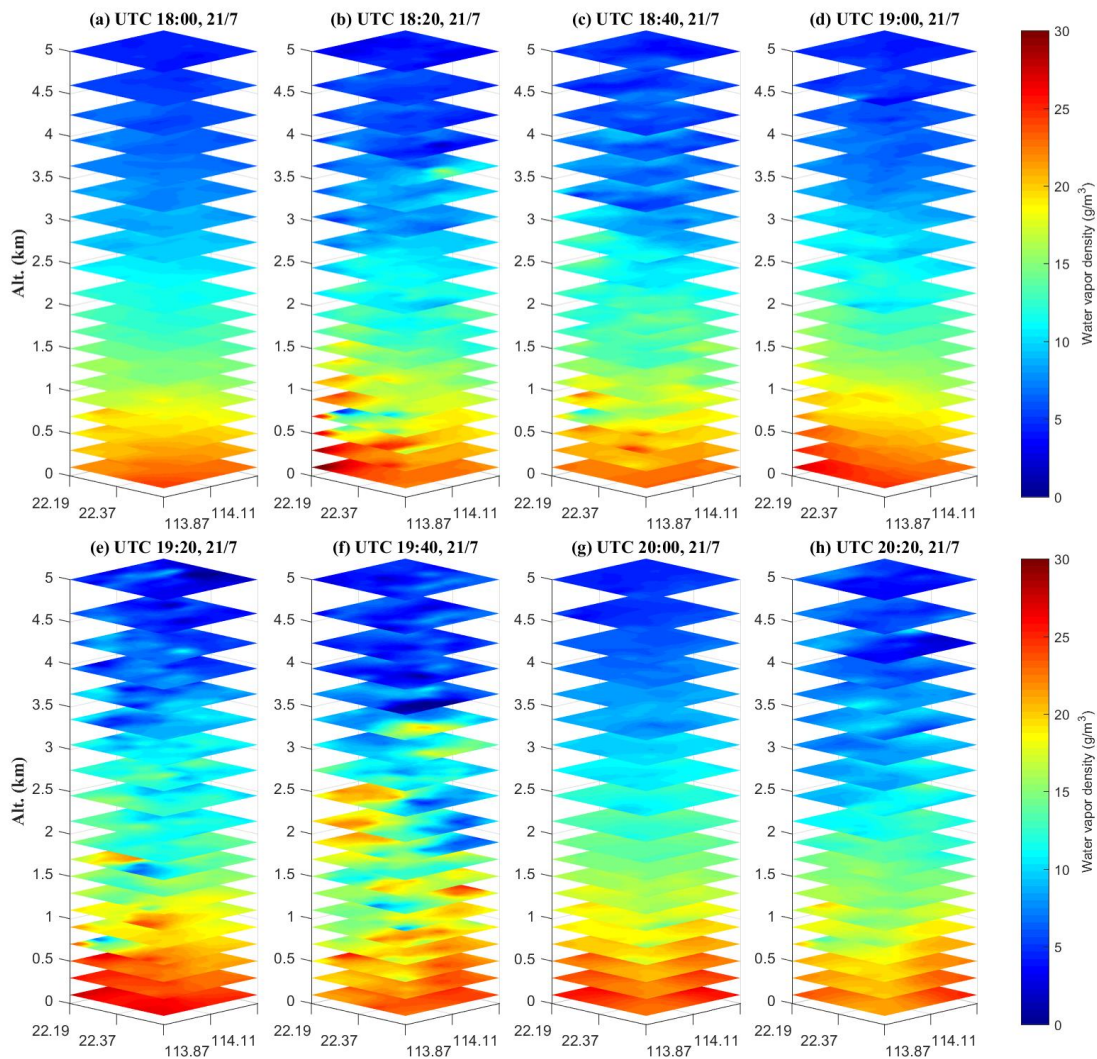
388 Figure 7. Distribution of water vapor density (WVD) profiles from GNSS tomographic result with
 389 the temporal resolution of 20 minutes for the location of PEN rain gauge over the period of UTC
 390 00:20 to 03:20, 23 July 2015, the blue line represents the beginning epoch of precipitation



391

392 Figure 8. Distribution of water vapor density (WVD) profiles from GNSS tomographic result with
393 the temporal resolution of 20 minutes for the location of TMS rain gauge over the period of UTC
394 00:20 to 03:20, 23 July 2015, **the blue line represents the beginning epoch of precipitation**
395

396 The 4-d distribution of atmospheric water vapour for the period UTC 18:00 to 20:20, 21 July 2015
397 is presented with a spatio-temporal resolution of 20 minutes and 20 layers to an altitude of 5 km,
398 respectively (Figure 9). According to the hourly rainfall recordings at 45 rain gauges in this area,
399 most parts of the experimental area suffered heavy rainfall at UTC 20:00, 21 July 2015 that lasted
400 for several hours. It can be found from Figure 9 that the significant vertical motion of water vapour
401 observed over the period from UTC 18:00 to 19:40, and returns to its relatively stable condition at
402 UTC 20:00 but with a lower water vapour content in most layers. The main reason for this may be
403 water vapour transfer to the liquid water particles and icy hydrometeors, which have little impact
404 on the delay of satellite signals and cannot be reflected evidently by the GNSS technique. For the
405 period of heavy rainfall that occurred after UTC 20:00, the atmospheric water vapour profiles were
406 relatively stable with slight vertical variation in water vapour content. In addition, it can be
407 concluded that the place at which hydrometeors were generated in the lower atmosphere is possibly
408 where rainfall occurred. Therefore, where heavy rainfall occurred is possibly predictable before the
409 onset of rainfall according to the 4-d atmospheric water vapour variations at different altitudes
410 derived from GNSS tomography. It also can be found that there is the horizontal motion of
411 atmospheric water vapor as well in different layers, especially at the bottom layers. This is because
412 the happening of rainfall requires the enough water vapor supplement, the horizontal motion of
413 water vapor at the bottom layers implies the continuous water vapor transportation.



414

415 Figure 9. Three-dimensional distribution of atmospheric water vapor density derived from GNSS
 416 tomographic result with the temporal resolution of 20 minutes over the period of UTC 18:00 to
 417 20:20, 21 July 2015 with 20 layers from the ground to 5km

418

419 5 Conclusion

420 GNSS sensing water vapour is an effective, practical technique, which is able to reflect 2-d and 4-d
 421 atmospheric water vapour variations during the formation and lifecycle of heavy rainfall. 2-d PWV
 422 time series data derived from GNSS observations are first compared with hourly rainfall
 423 measurements, which reveals the continuous increasing trend in PWV before the onset of rainfall
 424 and returns to its average value after rainfall. In addition, it is also found that the variations of surface
 425 temperature and relative humidity have day-periodicity and are mainly caused by the variations in
 426 solar radiation during no rain periods, but their changes are disturbed by rainfall during rainfall

427 periods.

428 A 4-d water vapour reconstruction technique is performed using GNSS data to analyse the vertical
429 water vapour movement during rainfall period. It is found that significant vertical motion occurred
430 about 1-2 hours before the arrival of rainfall and this was reflected by the ascending and descending
431 motions of water vapour in the lower and upper atmosphere, respectively. Hydrometeors are then
432 formed at a certain altitude where sufficient water vapour was concentrated. The formation of
433 hydrometeors and raindrops requires some time, which makes it possible for the forecasting of now-
434 casting rainfall. At the moment of onset of rainfall, the water vapour profiles return to their average
435 values at different altitudes and show a relative stable condition but with a decreasing trend in the
436 water vapour content in the lower atmosphere. In addition, the place where the rainfall is most
437 possible happened may be forecasted by locating out the location of the point of decreasing water
438 vapour content in the lower atmosphere. These results revealed that rainfall had a direct relationship
439 with atmospheric water vapour content as well as the vertical variations of water vapour density
440 profiles, which further manifested the significant potential of the GNSS technique for monitoring
441 and forecasting during the lifecycle of rainfall event.

442

443

444 **Acknowledgement:** The authors would like to thank IGAR for providing access to the web-based
445 IGAR data. The Lands Department of HKSAR is also acknowledge for providing GNSS and
446 meteorological data from the Hong Kong Satellite Positioning Reference Station Network (SatRef)
447 and the corresponding rainfall data. This research was supported by the Key projects of National
448 Natural Science Foundation (41730109).

449

450 **References:**

- 451 Akilan A.; Azeez K K A.; Balaji S, et al. GPS derived Zenith Total Delay (ZTD) observed at tropical locations in
452 South India during atmospheric storms and depressions. *Journal of Atmospheric and Solar-Terrestrial Physics*. 2015,
453 125, 1-7.
- 454 Alshawaf, F. Constructing water vapor maps by fusing InSAR, GNSS and WRF data. Karlsruhe, Karlsruher Institut
455 für Technologie (KIT), Dissertation. 2013.
- 456 Askne J.; Nordius H. Estimation of tropospheric delay for microwaves from surface weather data[J]. *Radio Science*.
457 1987, 22(03), 379-386.
- 458 Bai, Z. "Near-real-time GPS sensing of atmospheric water vapour," Ph.D. dissertation, Queensland Univ. of

459 Technol., Brisbane, Queensland, 2004

460 Barindelli, S.; Realini, E., Venuti, G.; Fermi, A & Gatti, A. Detection of water vapor time variations associated with
461 heavy rain in northern Italy by geodetic and low-cost GNSS receivers. *Earth Planets & Space*, 2018, 70(1), 28.

462 Bender M.; Raabe A. Preconditions to ground based GPS water vapour tomography. *Annales geophysicae*. 2007,
463 25(8), 1727-1734.

464 Bender M.; Stosius R.; Zus F.; et al. GNSS water vapour tomography—Expected improvements by combining GPS,
465 GLONASS and Galileo observations. *Advances in Space Research*. 2011, 47(5), 886-897.

466 Bender M.; Dick G.; Ge M.; et al. Development of a GNSS water vapour tomography system using algebraic
467 reconstruction techniques. *Advances in Space Research*, 2011, 47(10), 1704-1720.

468 Benevides P.; Catalao J.; Miranda P M A. On the inclusion of GPS precipitable water vapour in the nowcasting of
469 rainfall. *Natural Hazards and Earth System Sciences*. 2015b, 15(12), 2605-2616.

470 Benevides P.; Nico G.; Catalao J.; et al. Merging SAR interferometry and GPS tomography for high-resolution
471 mapping of 3D tropospheric water vapour. *Geoscience and Remote Sensing Symposium (IGARSS), 2015 IEEE*
472 *International*. IEEE, 2015a, 3607-3610.

473 Bennitt G V.; Jupp A. Operational assimilation of GPS zenith total delay observations into the Met Office numerical
474 weather prediction models. *Monthly Weather Review*, 2012, 140(8), 2706-2719.

475 Bevis M.; Businger S.; Herring T A.; et al. GPS meteorology: Remote sensing of atmospheric water vapor using the
476 Global Positioning System. *Journal of Geophysical Research: Atmospheres*. 1992, 97(D14), 15787-15801.

477 Bevis M.; Businger S.; Chiswell S.; et al. GPS meteorology: Mapping zenith wet delays onto precipitable water[J].
478 *Journal of applied meteorology*, 1994, 33(3), 379-386.

479 Bi Y.; Mao J.; Li C. Preliminary results of 4-D water vapor tomography in the troposphere using GPS. *Advances in*
480 *atmospheric sciences*, 2006, 23(4), 551-560.

481 Bock, O., Willis, P., WaDng, J., Mears, C. A high-quality, homogenized, global, long-term (1993–2008) DORIS
482 precipitable water data set for climate monitoring and model verification, *Journal of Geophysical Research*, 119,
483 7209–7230, doi:10.1002/2013JD021124, 2014

484 Böhm, J., Niell, A., Tregoning, P., & Schuh, H. (2006). Global Mapping Function (GMF): A new empirical mapping
485 function based on numerical weather model data. *Geophysical Research Letters*, 33(7).

486 Braun, John Joseph. Remote sensing of atmospheric water vapor with the global positioning system. *Geophysical*
487 *Research Letters*, 2004, 20(23), 2631-2634.

488 Braun J.; Rocken C.; Liljegren J. Comparisons of line-of-sight water vapor observations using the global positioning
489 system and a pointing microwave radiometer. *Journal of Atmospheric and Oceanic Technology*, 2003, 20(5), 606-
490 612.

491 Brenot H.; Neméghaire J.; Delobbe L.; et al. Preliminary signs of the initiation of deep convection by GNSS.
492 *Atmospheric Chemistry and Physics*, 2013, 13(11), 5425-5449.

493 Brenot, H., Ducrocq, V., Walpersdorf, A., Champollion, C., & Caumont, O. (2006). GPS zenith delay sensitivity
494 evaluated from high - resolution numerical weather prediction simulations of the 8 - 9 September 2002 flash flood
495 over southeastern France. *Journal of Geophysical Research: Atmospheres*, 111(D15).

496 Chen B, Liu Z. Voxel-optimized regional water vapor tomography and comparison with radiosonde and numerical
497 weather model. *Journal of geodesy*, 2014, 88(7), 691-703.

498 Dach, R., Lutz, S., Walser, P., Fridez, P., 2015. Bernese GNSS Software Version 5.2. Astronomical Institute,
499 University of Bern, 884.

500 Flores A.; Ruffini G.; Rius A. 4D tropospheric tomography using GPS slant wet delays//*Annales Geophysicae*.
501 *Springer-Verlag*, 2000, 18(2), 223-234.

502 Gradinarsky, L. P., Johansson, J., Bouma, H. R., Scherneck, H. G., Elgered, G. Climate monitoring using GPS,
503 *Physics and Chemistry of the Earth*, 27, 335–340, doi:10.1016/S1474-7065(02)00009-8, 2002.

504 Guerova G.; Jones J.; Dousa J.; et al. Review of the state of the art and future prospects of the ground-based GNSS
505 meteorology in Europe. *Atmospheric Measurement Techniques*, 2016, 9(11), 1-34.

506 Heublein M.; Zhu X X.; Alshawaf F.; et al. Compressive sensing for neutrospheric water vapor tomography using
507 GNSS and InSAR Observations[C]//Geoscience and Remote Sensing Symposium (IGARSS), 2015 *IEEE*
508 *International*. IEEE, 2015, 5268-5271.

509 Herring, T.A., King, R.W., McClusky, S.C., 2010. Documentation of the GAMIT GPS Analysis Software Release
510 10.4. Department of Earth and Planetary Sciences, Massachusetts Institute of Technology, Cambridge,
511 Massachusetts.

512 Hirahara K. Local GPS tropospheric tomography. *Earth, planets and space*, 2000, 52(11), 935-939.

513 JMA (2013) Outline of the operational numerical weather prediction at the Japan Meteorological Agency. Appendix
514 to WMO technical progress report on the global data-processing and forecasting system (GDPFS) and numerical
515 weather prediction (NWP) research. [http://www.jma.go.jp/jma/jma-eng/jma-center/nwp/outline2013-](http://www.jma.go.jp/jma/jma-eng/jma-center/nwp/outline2013-nwp/index.htm)
516 [nwp/index.htm](http://www.jma.go.jp/jma/jma-eng/jma-center/nwp/outline2013-nwp/index.htm). Accessed 30 Aug 2017

517 Kacmarik, M., Douša, J., Dick, G., Zus, F., Brenot, H., Möller, G., Pottiaux, E., Kaplan, J., Hordyniec, P., Václavovic,
518 P., Morel, L. Inter-technique validation of tropospheric slant total delays, *Atmospheric Measurement Techniques*,
519 10, 2183-2208, doi:10.5194/amt-10-2183-2017, 2017

520 Liu J.; Yao Y.; Sang J. A new weighted mean temperature model in China. *Advances in Space Research*, 2018, 61(1),
521 402-412.

522 Liu Z.; Wong M S.; Nichol J.; et al. A multi-sensor study of water vapour from radiosonde, MODIS and AERONET:
523 a case study of Hong Kong. *International Journal of Climatology*, 2013, 33(1), 109-120.

524 Ning, T. a Elgered, G. Trends in the atmospheric water vapour content from ground-based GPS: the impact of the
525 elevation cutoff angle, *IEEE Journal of Selected Topics in Applied Earth Observations and Remote Sensing*, 5, 744–
526 751, doi:10.1109/JSTARS.2012.2191392, 2012.

527 Perler D.; Geiger A.; Hurter F. 4D GPS water vapor tomography: new parameterized approaches. *Journal of Geodesy*,
528 2011, 85(8), 539-550.

529 Rius A.; Ruffini G.; and Cucurull L.; “Improving the vertical resolution of ionospheric tomography with GPS
530 occultations,” *Geophys. Res. Lett.* 1997, 24(18), 291–2294.

531 Rohm, W.: The ground GNSS tomography – unconstrained approach, *Advances in Space Research*, 51, 501–513,
532 doi:10.1016/j.asr.2012.09.021, 2013

533 Rohm W, Bosy J. Local tomography troposphere model over mountains area. *Atmospheric Research*, 2009, 93(4),
534 777-783.

535 Rohm W.; Bosy J. The verification of GNSS tropospheric tomography model in a mountainous area . *Advances in*
536 *Space Research*, 2011, 47(10), 1721-1730.

537 Saastamoinen, J. Atmospheric correction for the troposphere and stratosphere in radio ranging satellites. *The use of*
538 *artificial satellites for geodesy*, 1972, 247-251.

539 Saito K.; Shoji Y.; Origuchi S.; et al. GPS PWV Assimilation with the JMA Nonhydrostatic 4DVAR and Cloud
540 Resolving Ensemble Forecast for the 2008 August Tokyo Metropolitan Area Local Heavy Rainfalls//*Data*
541 *Assimilation for Atmospheric, Oceanic and Hydrologic Applications (Vol. III)*. Springer, Cham, 2017, 383-404.

542 Shoji, Y. (2009). Assimilation of nationwide and global gps pwv data for a heavy rain event on 28 july 2008 in
543 hokuriku and kinki, japan. *SOLA - Scientific Online Letters on the Atmosphere*, 5(1), 45-48.

544 Shoji, Y. (2013). Retrieval of water vapor inhomogeneity using the japanese nationwide gps array and its potential
545 for prediction of convective precipitation. *Journal of the Meteorological Society of Japan*, 91(1), 43-62.

546 Shanguan, M., Bender, M., Ramatschi, M., Dick, G., Wickert, J., Raabe, A., Galas, R.
547 GPS tomography: validation of reconstructed 3-D humidity fields with radiosonde profiles, *Annales Geophysicae*,
548 31, 1491-1505, doi:10.5194/angeo-31-1491-2013, 2013.

549 Skone S.; Hoyle V. Troposphere Modeling in a Regional GPS Network. *Positioning*, 2005, 4(1&2), 230-239.

550 Troller M.; Geiger A.; Brockmann E.; et al. Determination of the spatial and temporal variation of tropospheric water
551 vapour using CGPS networks. *Geophysical Journal International*, 2006, 167(2), 509-520.

552 Vey, S., Dietrich, R., Rülke, A., Fritsche, M., Steigenberger, P., Rothacher, M.: Validation of precipitable water
553 vapour within the NCEP/DOE reanalysis using global GPS observations from one decade, *Journal of Climate*, 23,
554 1675–1695, doi:10.1175/2009JCLI2787.1, 2010.

555 Wang, X., Wang, X., Dai, Z., et al. Tropospheric wet refractivity tomography based on the BeiDou satellite system.
556 *Advances in Atmospheric Sciences*, 2014, 31(2), 355-362.

557 Wu, D., Zhao, X., Liang, S., Zhou, T., Huang, K., Tang, B., and Zhao W. (2015). Time-lag effects of global
558 vegetation responses to climate change. *Global Change Biology*, 21(9), 3520-3531.

559 Yao Y B.; Zhu S.; Yue S Q. A globally applicable, season-specific model for estimating the weighted mean
560 temperature of the atmosphere. *Journal of Geodesy*, 2012, 86(12), 1125-1135.

561 Yao Y B.; Zhao Q Z.; Zhang B. A method to improve the utilization of GNSS observation for water vapor
562 tomography. *Annales Geophysicae (09927689)*, 2016, 34(1), 143-152.

563 Yao Y.; Zhao Q. Maximally Using GPS Observation for Water Vapor Tomography. *IEEE Transactions on*
564 *Geoscience and Remote Sensing*, 2016, 54(12), 7185-7196.

565 Yao Y.; Zhao Q. A novel, optimized approach of voxel division for water vapor tomography[J]. *Meteorology and*
566 *Atmospheric Physics*, 2017, 129(1), 57-70.

567 Yao Y.; Shan L.; Zhao Q. Establishing a method of short-term rainfall forecasting based on GNSS-derived PWV
568 and its application. *Scientific reports*, 2017, 7(1), 12465.

569 Yao Y.; Zhang B.; Xu C. and Yan, F. Improved one/multi-parameter models that consider seasonal and geographic
570 variations for estimating weighted mean temperature in ground-based GPS meteorology. *Journal of Geodesy*, 2014,
571 88(3), 273-282.

572 Yao Y B.; Liu J H.; Zhang B.; et al. Nonlinear relationships between the surface temperature and the weighted mean
573 temperature. *Geomatics & Information Science of Wuhan University*, 2015, 40(1), 112-116.

574 Zhang K.; Manning T.; Wu S.; et al. Capturing the signature of severe weather events in Australia using GPS
575 measurements. *IEEE Journal of Selected Topics in Applied Earth Observations and Remote Sensing*, 2015, 8(4),
576 1839-1847.

577 Zhao Q.; Yao Y. An improved troposphere tomographic approach considering the signals coming from the side face
578 of the tomographic area//Annales Geophysicae. *Copernicus GmbH*, 2017b, 35(1), 87-95.

579 Zhao Q.; Yao Y.; Cao X.; et al. Accuracy and reliability of tropospheric wet refractivity tomography with GPS, BDS,
580 and GLONASS observations. *Advances in Space Research*, 2018c. DOI:10.1016/j.asr.2018.01.021

581 Zhao Q.; Yao Y.; Yao W. A troposphere tomography method considering the weighting of input
582 information[C]//Annales Geophysicae. *Copernicus GmbH*, 2017a, 35(6), 1327-1340.

583 Zhao Q.; Yao Y.; Yao W. GPS-based PWV for precipitation forecasting and its application to a typhoon event.
584 *Journal of Atmospheric and Solar-Terrestrial Physics*, 2018a, 167, 124-133.

585 Zhao Q., Yao Y., Cao X., Zhou F. and Xia P. An Optimal Tropospheric Tomography Method Based on the Multi-
586 GNSS Observations. *Remote Sensing*, 2018d, 10(2), 234.

587 Zhao Q.; Yao Y.; Yao W.; et al. Real-time precise point positioning-based zenith tropospheric delay for precipitation
588 forecasting. *Scientific reports*, 2018b, 8(1), 7939-7939.

589 Zhao, Q., Yao, Y., Yao, W. Q., & Li, Z. Near-global GPS-derived PWV and its analysis in the El Niño event of
590 2014–2016. *Journal of Atmospheric and Solar-Terrestrial Physics*, 2018e, 179, 69-80.